

High-mobility three-atom-thick semiconducting films with wafer-scale homogeneity

Kibum Kang¹*, Saien Xie²*, Lujie Huang¹, Yimo Han², Pinshane Y. Huang², Kin Fai Mak^{3,4}, Cheol-Joo Kim¹, David Muller^{2,3} & Jiwoong Park^{1,3}

The large-scale growth of semiconducting thin films forms the basis of modern electronics and optoelectronics. A decrease in film thickness to the ultimate limit of the atomic, sub-nanometre length scale, a difficult limit for traditional semiconductors (such as Si and GaAs), would bring wide benefits for applications in ultrathin and flexible electronics, photovoltaics and display technology¹⁻³. For this, transition-metal dichalcogenides (TMDs), which can form stable three-atom-thick monolayers4, provide ideal semiconducting materials with high electrical carrier mobility⁵⁻¹⁰, and their largescale growth on insulating substrates would enable the batch fabrication of atomically thin high-performance transistors and photodetectors on a technologically relevant scale without film transfer. In addition, their unique electronic band structures provide novel ways of enhancing the functionalities of such devices, including the large excitonic effect11, bandgap modulation12, indirect-todirect bandgap transition¹³, piezoelectricity¹⁴ and valleytronics¹⁵. However, the large-scale growth of monolayer TMD films with spatial homogeneity and high electrical performance remains an unsolved challenge. Here we report the preparation of high-mobility 4-inch wafer-scale films of monolayer molybdenum disulphide (MoS₂) and tungsten disulphide, grown directly on insulating SiO₂ substrates, with excellent spatial homogeneity over the entire films. They are grown with a newly developed, metal-organic chemical vapour deposition technique, and show high electrical performance, including an electron mobility of 30 cm²V⁻¹s⁻¹ at room temperature and 114 cm² V⁻¹ s⁻¹ at 90 K for MoS₂, with little dependence on position or channel length. With the use of these films we successfully demonstrate the wafer-scale batch fabrication of highperformance monolayer MoS₂ field-effect transistors with a 99% device yield and the multi-level fabrication of vertically stacked transistor devices for three-dimensional circuitry. Our work is a step towards the realization of atomically thin integrated circuitry.

Existing growth methods for large-scale monolayer TMDs have so far produced materials with limited spatial uniformity and electrical performance. For instance, the sulphurization of metal or metal compounds only provides control over the average layer number, producing spatially inhomogeneous mixtures of monolayer, multi-layer and no-growth regions ^{16,17}. Although chemical vapour deposition (CVD) based on solid-phase precursors (such as MoO₃, MoCl₅ or WO₃) ^{18–23} has shown better thickness control on a large scale, the electrical performance of the resulting material, which is often reported from a small number of devices in selected areas, fails to show spatially uniform high carrier mobility.

Here we report the growth of semiconducting monolayer films of MoS₂ and tungsten disulphide (WS₂) on silicon oxide on a 4-inch wafer scale, with both excellent electrical performance and structural continuity, maintained uniformly over the entire films. Figure 1 presents our continuous TMD monolayer films and shows their wafer-scale homogeneity and intrinsic optical properties. The colour photos of MoS₂ (Fig. 1a; greenish yellow) and WS₂ (Fig. 1b; yellow) films

grown on a transparent 4-inch fused silica wafer show that the TMD grown region (right half) is uniform over the whole substrate and clearly distinguishable from the bare silica substrate (left half). The optical absorption, photoluminescence and Raman spectra measured from our films show characteristics unique to monolayer MoS₂ and WS₂, respectively (Fig. 1d–f). All of these measured spectra have the same peak positions as in exfoliated monolayer samples (denoted by diamonds)^{13,24–26}, regardless of the location of the measurements within our films (Supplementary Fig. 1). The X-ray photoelectron spectra taken from our monolayer MoS₂ film show almost identical features to those of bulk single crystal with a low level of defects, further confirming the precise chemical composition and the high quality of our MoS₂ film (Supplementary Fig. 2).

Figure 1c shows a photo of a MoS₂ film grown on a 4-inch SiO₂/Si wafer. The monolayer film was patterned using standard photolithography and oxygen plasma etching to form MoS2-covered squares (dark, 6 mm wide) with an array of 3 µm holes. An enlarged, normalized optical reflection image (Fig. 1h) displays a homogeneous reflection contrast for the entire MoS₂-covered region, confirming uniform monolayer growth everywhere with no gaps. In addition, Fig. 1g shows a scanning electron microscope (SEM) image of an array of fully suspended monolayer MoS₂ membranes (2 μm in diameter) fabricated by transferring our metal-organic chemical vapour deposition (MOCVD)-grown film onto a SiN grid with holes. Its high fabrication yield (>99.5%) suggests mechanical strength and continuity of the film. The widefield photoluminescence images of these films (insets to Fig. 1g, h) show strong, spatially uniform photoluminescence signals, further confirming that they are continuous monolayer MoS₂, with its high quality maintained even after patterning or transfer. The same spatial uniformity was seen in the optical reflection and photoluminescence images of a monolayer WS2 film that was similarly grown and patterned (Fig. 1i). Together, the data in Fig. 1 confirm that our MoS₂ and WS₂ films are continuous monolayers, spatially uniform over the entire 4-inch growth substrates with intrinsic optical properties. Below, using MoS₂ as the main example, we discuss the growth (Fig. 2) and the excellent electrical properties (Fig. 3) of these MOCVD-grown films.

Figure 2a schematically explains our MOCVD growth, where we only use gas-phase precursors of Mo(CO)₆, W(CO)₆, (C_2H_5)₂S and H_2 , all diluted in argon as a carrier gas (see Supplementary Methods). The concentration of each reactant can be precisely controlled during the entire growth time by regulating the partial pressure (P_X) of each reactant X. Thus our setup offers an ideal environment for maximizing the areal coverage of the monolayer and for engineering the film structure by controlling the nucleation density and intergrain stitching. Figure 2 summarizes our key findings.

First, our MoS₂ film is grown in the layer-by-layer growth mode, which is ideal for uniform layer control over the large scale. Figure 2c plots the areal coverage of monolayer (θ_{1L}) and multilayer ($\theta_{\ge 2L}$; mostly bilayer) regions measured from our MoS₂ grown on SiO₂/Si;

¹Department of Chemistry and Chemical Biology, Cornell University, Ithaca, New York 14853, USA. ²School of Applied and Engineering Physics, Cornell University, Ithaca, New York 14853, USA. ³Kavli Institute at Cornell for Nanoscale Science, Ithaca, New York 14853, USA. ⁴Laboratory of Atomic and Solid State Physics, Cornell University, Ithaca, New York 14853, USA. ^{*}These authors contributed equally to this work.

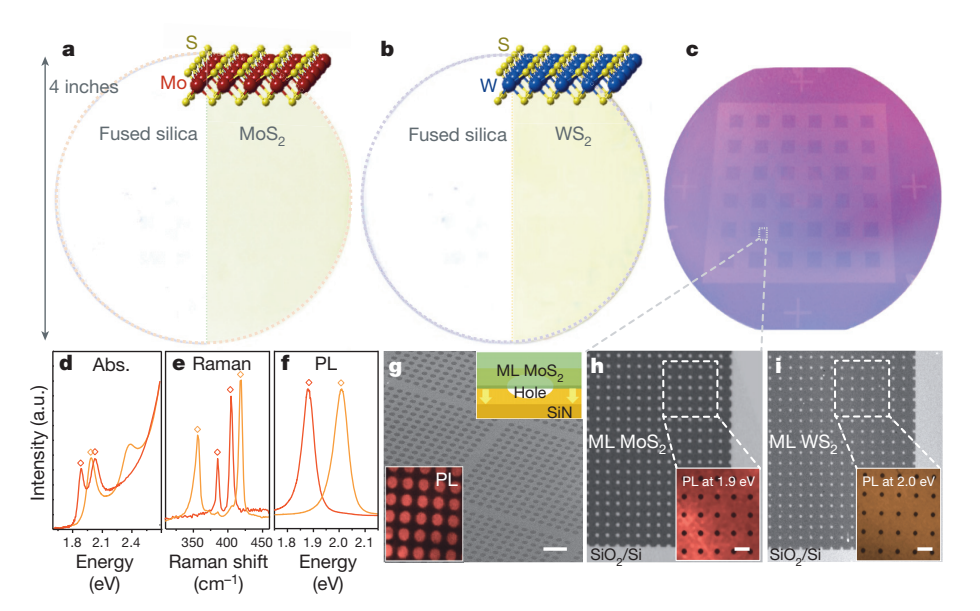


Figure 1 | Wafer-scale monolayer TMD films. a, b, Photographs of monolayer MoS_2 (a) and WS_2 (b) films grown on 4-inch fused silica substrates, with diagrams of their respective atomic structures. The left halves show the bare fused silica substrate for comparison. c, Photograph of patterned monolayer MoS_2 film on a 4-inch SiO_2/Si wafer (the darker areas are covered by MoS_2). d, Optical absorption spectra of MOCVD-grown monolayer MoS_2 (red line) and WS_2 (orange line) films in the photon energy range from 1.6 to 2.7 eV. e, Raman spectra of as-grown monolayer MoS_2 and WS_2 , normalized to the silicon peak intensity. f, Normalized photoluminescence spectra of

as-grown monolayer MoS₂ and WS₂. The peak positions in **d-f** are consistent with those seen from exfoliated samples (diamonds). **g**, SEM image and photoluminescence (PL) image (bottom inset, at 1.9 eV) of monolayer (ML) MoS₂ membranes suspended over a SiN TEM grid with 2 μ m holes (a diagram of the suspended film is shown in the top inset). Scale bar, 10 μ m. **h**, **i**, Optical images (normalized to the bare substrate region) of patterned monolayer MoS₂ (**h**) and WS₂ (**i**) on SiO₂, taken from the wafer-scale patterned films. The insets show photoluminescence images at 1.9 eV (**h**) and 2.0 eV (**i**). Scale bars, 10 μ m.

Fig. 2b shows optical images at different growth times, revealing the initial nucleation on the SiO₂ surface ($t = 0.5t_0$), subsequent monolayer growth near $(0.8t_0)$ and at the maximum monolayer coverage (t_0) , followed by nucleation mainly at grain boundaries $(1.2t_0)$ and bilayer growth $(2t_0)$. We observed no nucleation of a second layer while the first layer was forming $(\theta_{\geq 2L} \approx 0 \text{ when } t < t_0)$, producing an optimal growth time t_0 near full monolayer coverage $(\theta_{1L} \approx 1)$. Additional photoluminescence and electron microscope images taken after different growth times further suggested that the edge attachment was the main mechanism for the monolayer growth after nucleation and that the neighbouring monolayer grains were uniformly connected by tilt grain boundaries with enhanced photoluminescence¹⁹ at $t = t_0$ (see Supplementary Notes and Supplementary Figs 3 and 4). The standard thin-film growth model²⁷ suggests that this growth mode is effective below a certain deposition rate of the growth species, above which it suggests a different mode that forms thicker islands. Indeed, the layer-by-layer growth of MoS₂ film was observed only when we applied a low partial pressure ($P_{\text{Mo}} \approx 10^{-4} \,\text{Torr}$ in Fig. 2b, c) of Mo vapour (produced by the thermal decomposition of Mo(CO)₆; see Supplementary Notes and Supplementary Fig. 5) in the presence of excess $(C_2H_5)_2S$. In contrast, the growth at a higher P_{Mo} was no longer in the layer-by-layer growth mode, instead simultaneously producing a mixture of monolayer, multilayer and no-growth regions (Supplementary Fig. 6). For the uniform monolayer growth over a large substrate, it is thus important to maintain a low P_{Mo} constantly over the entire growth region and over time, the key technical capability provided by our MOCVD setup (see Supplementary Fig. 7 for the spatially homogeneous monolayer nucleation on a multi-inch scale).

Second, the grain structure of our MoS₂ film, including the average grain size and the intergrain connection, depends sensitively on the concentrations of H_2 , $(C_2H_5)_2S$ as well as residual water. As a representative example, Fig. 2d shows the two main effects of H_2 , whose presence is necessary for removing carbonaceous species generated during the MOCVD growth: the average grain size increases from hundreds of nanometres to more than $10 \, \mu m$ with decreasing H_2 flow, and the MoS₂ grains grown under higher H_2 flow (Fig. 2d, right image)

have mostly perfect triangular shapes without merging with neighbouring grains, a trend that disappears with lower H_2 flow (left and middle images). These observations are consistent with the H_2 -induced decomposition of $(C_2H_5)_2S$ (increasing nucleation due to hydrogenolysis)²⁸ and the etching of the MoS_2 (preventing intergrain connection)²⁹ as reported previously. (For further discussion on the effects of $(C_2H_5)_2S$ and water, see Supplementary Notes and Supplementary Fig. 6.) To grow continuous monolayer MoS_2 with a large grain size and high-quality intergrain stitching, we thus flowed optimal amounts of H_2 and $(C_2H_5)_2S$ and dehydrated the growth environment.

The darkfield transmission electron microscope (DF-TEM) and annular darkfield scanning TEM (ADF-STEM) images shown in Fig. 2e, f confirm the structural continuity of our MoS₂ film grown under those conditions on the nanometre and atomic length scales. The DF-TEM image shows a continuous polycrystalline monolayer film with no visible gaps and a bilayer area of less than 0.5%. Further analysis of the DF-TEM and electron diffraction data (see Supplementary Fig. 8) confirms a uniform angular distribution of crystal orientations with no preferred intergrain tilt angle for grain boundaries. The ADF-STEM data (Fig. 2f; more images are shown in Supplementary Fig. 9) further confirm that adjacent grains are likely to be connected by a high-quality lateral connection with structures similar to those seen in previous reports^{18,19}. The MoS₂ films shown in Fig. 1 as well as those whose electrical properties we show in Figs 3 and 4 were grown under the conditions described in Supplementary Methods, producing an average grain size of \sim 1 μm (see Fig. 2b, e). Almost identical growth parameters with $P_{\rm W} \approx 10^{-4}$ Torr produced monolayer WS2 films as shown in Fig. 1b, i, indicating the same layerby-layer growth for WS_2 with a similar t_0 .

The electrical properties of our monolayer MoS₂ films have two important characteristics: the spatial uniformity over a large scale and excellent transport properties similar to those seen in exfoliated samples. All our electrical measurements in Figs 3 and 4 (except those in Fig. 3c) were performed at room temperature. Figure 3a shows a plot of sheet conductance (σ_{\square}) against backgate voltage ($V_{\rm BG}$) measured from a monolayer MoS₂ field-effect transistor (FET; optical image

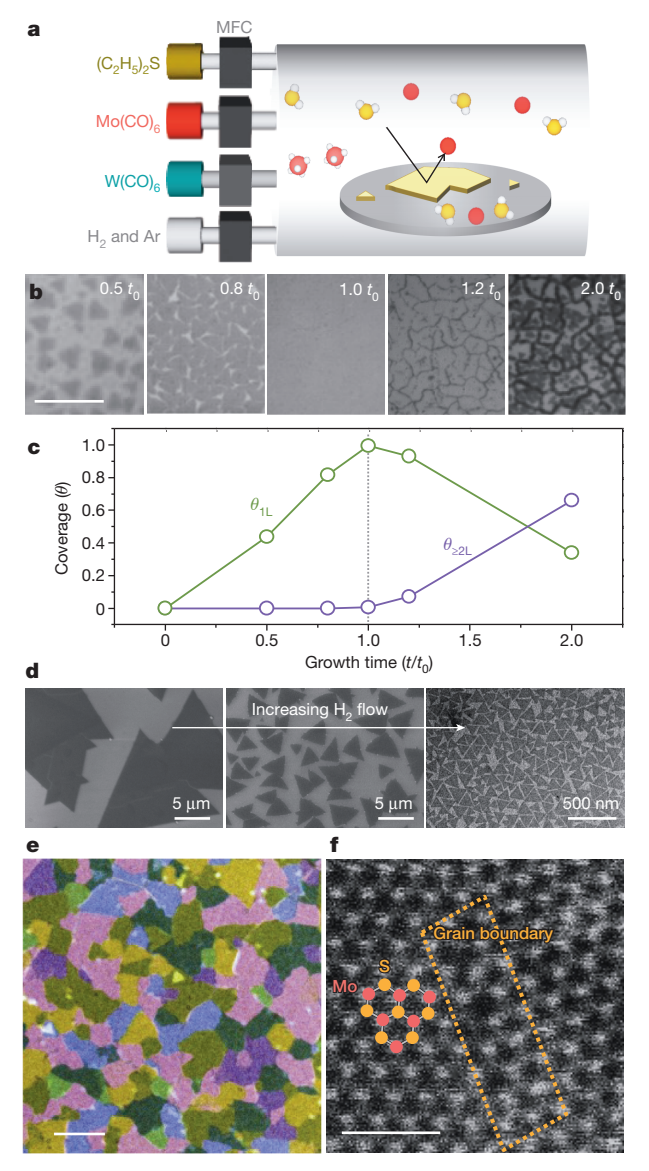


Figure 2 | MOCVD growth of continuous monolayer MoS₂ film. a, Diagram of our MOCVD growth setup. Precursors were introduced to the growth setup with individual mass flow controllers (MFCs). Red, Mo or W atom; yellow, S atom; white, carbonyl or ethyl ligand. b, Optical images of MOCVD-grown MoS₂ at the indicated growth times, where t_0 was the optimal growth time for full monolayer coverage. Scale bar, $10 \, \mu m$. c, Coverage ratio for monolayer (θ_{1L} , green) and multi-layer ($\theta_{≥2L}$, purple) regions as a function of growth time. d, Grain size variation of monolayer MoS₂ depending on the hydrogen flow rate; from left to right, 5 standard cm³ min⁻¹ (sccm) (SEM image shown), 20 sccm (SEM) and 200 sccm (TEM). e, False-colour DF-TEM image showing a continuous monolayer MoS₂ film. Scale bar, 1 μm. f, ADF-STEM image of a laterally stitched grain boundary in a monolayer MoS₂ film, with red and yellow dots representing the Mo and S atoms, respectively. Scale bar, 1 nm.

shown in the inset) with multiple electrodes for the four-probe measurements (except for a channel length L of 34 μ m). It includes several curves for different L ranging between 1.6 and 34 μ m (shifted from the bottom curve for clarity), all of which show nearly identical behaviours, including the n-type conductance, carrier concentration ($\sim 4 \times 10^{12} \, \mathrm{cm}^{-2}$ at $V_{\mathrm{BG}} = 0 \, \mathrm{V}$) and high field-effect mobility (μ_{FE}). Figure 3b further plots μ_{FE} measured from five such devices, fabricated at random locations and separated by up to 3.3 mm on a single chip. All the devices show similar μ_{FE} near 30 cm 2 V $^{-1}$ s $^{-1}$, independent of L and device location, with similarly uniform $\sigma_{\Box} - V_{\mathrm{BG}}$ curves (shown in Supplementary Fig. 10), suggesting the spatial homogeneity of the

electrical properties of the MoS₂ film at length scales ranging from micrometres to millimetres.

The distribution of μ_{FE} of our devices is compared with the results of multiple devices from two previous reports, each measured from individual grains of exfoliated or CVD-grown MoS2 samples. We find that $\mu_{\rm FE}$ measured from our MOCVD film is similar to the median $\mu_{\rm FE}$ (denoted by a star) of exfoliated samples (and several times higher than the CVD results) and has a much narrower distribution. In addition, the temperature dependence of $\mu_{\rm FE}$ (Fig. 3c) measured from the same device in Fig. 3a shows higher $\mu_{\rm FE}$ at lower temperatures (92 cm² V⁻¹ s⁻¹ at 100 K) and intrinsic, phonon-limited electron transport similar to the behaviours previously observed in exfoliated samples (data from ref. 6 shown in Fig. 3c) but different from those observed from a CVD sample with stronger effects from defects³⁰. Specifically, our data show that the temperature dependence of mobility follows a power law of $\mu_{\rm FE} \approx T^{-\gamma}$ with exponent $\gamma = 1.6$ for temperatures between 150 and 300 K, close to the value (1.69) predicted by theory⁵ and consistent with results from previous experiments (average value ranging between 0.6 and 1.7)⁶⁻⁹ for a similar temperature range. Finally, Fig. 3d shows a high-performance MoS_2 FET fabricated with an individual top-gate electrode (V_{TG}). It has a high on/off conductance ratio ($\sim 10^6$), current saturation at relatively low bias $V_{\rm SD}$ (lower inset to Fig. 3d), high field-effect mobility (~29 cm² V⁻¹ s⁻¹) and large transconductance (~2 μ S μ m⁻¹), all of which are comparable to the best reported results⁶⁻⁸. We note that our devices studied in Fig. 3a-d were fabricated at random locations using a polycrystalline monolayer MoS₂ film, unlike the devices with singlegrain samples used for comparison. In addition, the electrical properties measured from a separate monolayer MoS₂ film with a larger average grain size of 3 µm (instead of 1 µm in Fig. 3) have almost identical characteristics, including the channel-length independence of μ_{FE} and the phonon-limited transport at T > 150 K (see Supplementary Fig. 11; with the low-temperature mobility as high as 114 cm² V⁻¹ s⁻¹ at 90 K). Taken together, our data confirm the spatial uniformity and high electrical performance of our MoS₂ FETs independent of the average grain size, which suggests that the intergrain boundaries in our film do not significantly degrade their electrical transport properties. This is probably due to the formation of well-stitched intergrain boundaries with a low level of defects, an explanation also supported by the ADF-STEM (Fig. 2f) and X-ray photoelectron spectrum data (Supplementary Fig. 2) discussed above. Our data therefore lead us to conclude that our optimized MOCVD growth provides an electrically homogeneous monolayer MoS₂ film. Moreover, we successfully fabricated and measured 60 FETs by using a monolayer WS2 film. Even though the growth of monolayer WS2 was not carefully optimized, these devices showed excellent electrical properties, with their $\mu_{\rm FE}$ as high as $18\,{\rm cm}^2{\rm V}^{-1}\,{\rm s}^{-1}$ at room temperature (Fig. 3e) and a median $\mu_{\rm FE}$ close to 5 cm² V⁻¹ s⁻¹. In addition, the WS₂ device in Fig. 3e showed a high on/off ratio of 10⁶ and the current saturation behaviour (inset to Fig. 3e) as in our MoS₂ devices. (See Supplementary Fig. 12 for data from additional monolayer WS₂ FET devices).

The structural and electrical uniformity of our MoS₂ film enables the wafer-scale batch fabrication of high performance FETs as demonstrated in Fig. 3f, g. Figure 3f shows a photo of 8,100 MoS₂ FETs with a global back gate, which were fabricated on a 4-inch SiO₂/Si wafer with a standard photolithography process. The middle and bottom insets to Figure 3f show colour-scale maps of σ_{\square} measured from 100 MoS₂ FETs in one square region at $V_{\rm BG} = +50 \, \rm V$ and $-50 \, \rm V$, respectively; the top inset to Fig. 3f shows an enlarged optical image of the devices. We observed an almost perfect device yield of 99%; only two out of 200 FETs that we characterized (including data from an adjacent region) did not conduct. Our data also confirm the spatially uniform n-type transistor operation (larger σ_{\square} for positive V_{BG}) with similar V_{BG} dependence for all our devices and high on-state device conductance. We further observed similarly uniform $V_{\rm BG}$ dependence from FET devices fabricated using monolayer MoS₂ films with different average grain sizes, as characterized by the histograms of the threshold voltages

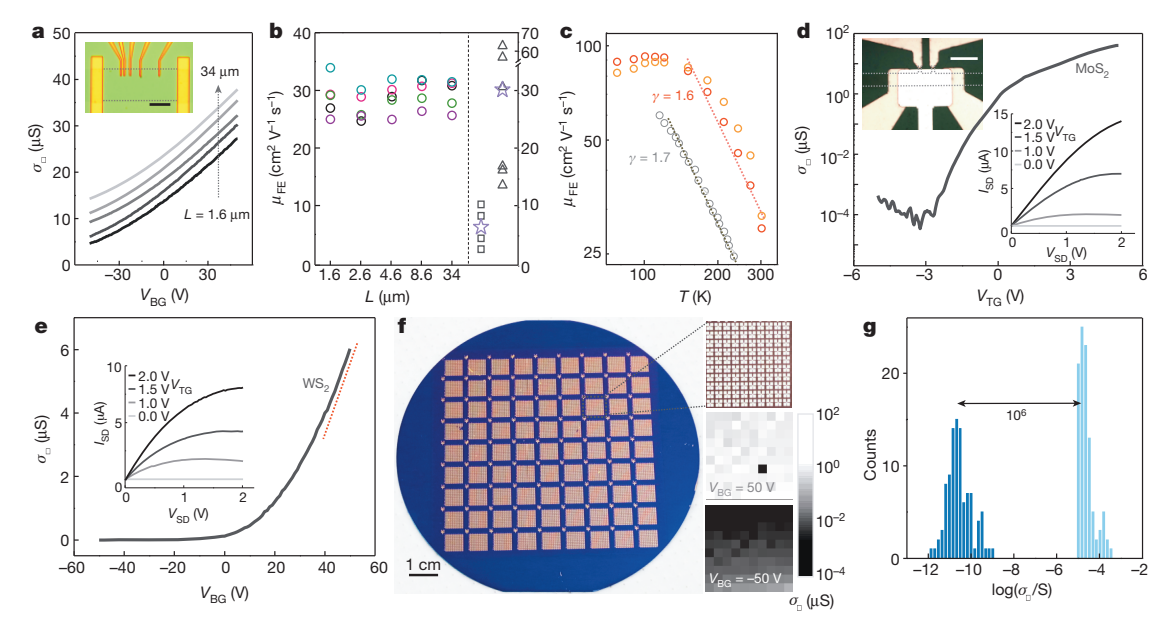


Figure 3 | Electrical characterization and batch fabrication of monolayer TMD FETs. a, Gate-dependent sheet conductance (σ_{\square}) of monolayer MoS₂ FETs measured at different channel lengths L (curves displaced from the bottom for clarity). Inset: optical image of the device; scale bar, $10~\mu m$. b, Field-effect mobility ($\mu_{\rm FE}$) measured from five MoS₂ FETs (ellipses) fabricated at random locations with different L. Data from previous results for CVD-grown samples²¹ (squares) and exfoliated samples⁷ (triangles) are shown for comparison (purple stars indicate their medians). c, Temperature dependence of $\mu_{\rm FE}$ measured from the device in Fig. 3a at $L=1.6~\mu m$ (orange) and $8.6~\mu m$ (red), and from a previous report on exfoliated samples⁶ (grey), both showing phonon-limited intrinsic transport. d, Top gate ($V_{\rm TG}$)-dependent σ_{\square} for dual-gate monolayer MoS₂ FET (device shown in the upper inset). Lower inset:

 $V_{\rm TG}$ -dependent $I_{\rm SD}-V_{\rm SD}$ curves showing current saturation and ohmic electrode contact. Scale bar, $10~\mu{\rm m}$. e, Gate-dependent σ_{\square} of a monolayer WS $_2$ FET showing $\mu_{\rm FE}=18~{\rm cm}^2~{\rm V}^{-1}~{\rm s}^{-1}$. Inset: $V_{\rm TG}$ -dependent $I_{\rm SD}-V_{\rm SD}$ curves showing current saturation and ohmic electrode contact. f, Batch-fabricated 8,100 MoS $_2$ FET devices on a 4-inch SiO $_2$ /Si wafer. Top inset: enlarged image of one square containing 100 devices. Middle and bottom insets: corresponding colour maps of σ_{\square} at gate bias $V_{\rm BG}=50~{\rm V}$ and $-50~{\rm V}$, respectively, with the black block in the middle inset representing the only non-conducting device. g, Histogram of on-state and off-state σ_{\square} of 100 dual-gate FETs showing a median on–off ratio of 10^6 and a high on-state conductivity. Dark blue, $V_{\rm TG}=-5~{\rm V}$; pale blue, $V_{\rm TG}=+5~{\rm V}$. All measurements were performed at room temperatures except those in c.

(Supplementary Fig. 13). Similarly, we fabricated 100 individually addressable dual-gate MoS₂ FETs (similar to the device in Fig. 3d) on another wafer piece. The histogram of the on-state σ_{\square} ($V_{TG} = 5$ V; median carrier concentration $\sim 7 \times 10^{12}$ cm⁻²) and off-state σ_{\square} ($V_{TG} = -5$ V) collected from all such FETs (Fig. 3g) shows strong peaks above 10^{-5} S and near 10^{-11} S, respectively, confirming a uniform conductance switching behaviour with high on-state σ_{\square} (>10 µS) and on-off ratio ($\sim 10^6$). In addition, most of these batch-fabricated FETs had a high μ_{FE} (>10 cm² V⁻¹ s⁻¹; see Supplementary Fig. 14).

The data presented in Figs 1-3 confirm the structural and electrical uniformity of the wafer-scale monolayer MoS_2 film grown by our MOCVD method. This makes our film compatible with batch device fabrication processes on a technologically relevant scale. Moreover, because SiO_2 provides a substrate for its growth, one can produce high-quality monolayer films on a variety of substrates by depositing SiO_2 before the growth. This versatility would permit the fabrication of high-performance FETs directly on non-conventional substrates, such as metal and thermally stable plastic. In addition, one can integrate multiple layers of MoS_2 devices by repeating the TMD film growth, device fabrication and SiO_2 deposition, which could enable novel three-dimensional circuitry.

In Fig. 4 we demonstrate this unique potential by producing multi-stacked monolayer MoS₂ films as well as electronic devices fabricated at different vertical levels. Figure 4a shows diagrams and photographs of three substrates each with single, double or triple monolayer MoS₂ films grown at different levels. The first (bottom) monolayer film was grown on a fused silica substrate; the additional layers were grown on SiO₂ (100 nm thick) deposited on the previously grown MoS₂ monolayer by using plasma-enhanced CVD. The colour of the substrate, which remains uniform for each substrate, becomes darker as the number of layers increases. Their absorption spectra, shown in Fig. 4b, present almost identical absorption at all

measured wavelengths, once normalized by the number of stacks grown (see the inset), suggesting little degradation of the optical properties of the monolayer MoS_2 films after subsequent oxide deposition and MoS_2 growth.

Figure 4c shows successive diagrams of our multi-stacked device fabrication process: growth of the first MoS₂ monolayer on a SiO₂/ Si wafer, FET fabrication, deposition of SiO₂ (thickness 500 nm; see Supplementary Methods for details), and growth of the second MoS₂ monolayer and FET fabrication. A false-colour SEM image in Fig. 4d shows an array of MoS₂ FETs successfully fabricated with this process. It includes functioning MoS₂ FETs located at two different vertical levels whose conductance can be simultaneously modulated with a global back gate. The $I_{\rm SD}\text{-}V_{\rm SD}$ curves measured from two FETs, adjacent both laterally and vertically (see the inset to Fig. 4d), are shown in Fig. 4e. Both devices show a $V_{\rm BG}$ -dependent conductance change (notice the smaller change for the second layer) with an on-state σ_{\square} of 2.5 μ S (first layer) and 1.5 μ S (second layer), respectively. Furthermore, we measured similar $\mu_{\rm FE}$ values (11.5 and $8.8 \,\mathrm{cm}^2 \,\mathrm{V}^{-1} \,\mathrm{s}^{-1}$) from the two devices (Supplementary Fig. 15). The two monolayer MoS₂ films were grown on SiO₂ substrates prepared differently, and the first-layer device had gone through additional steps, including the second MoS₂ growth. Our data in Fig. 4 thus confirm the compatibility of our MOCVD-grown MoS₂ films with conventional thin-film deposition and multistacking, which could be used to develop a three-dimensional device architecture based on TMD.

Our high-mobility monolayer TMD films can be used immediately for the batch fabrication of TMD-based integrated circuitry consisting of FETs, photodetectors and light emitting diodes, on a technologically relevant multi-inch wafer scale. In addition, because our MOCVD growth is controlled by the kinetics of precursor supply rather than specific precursor-substrate chemistry

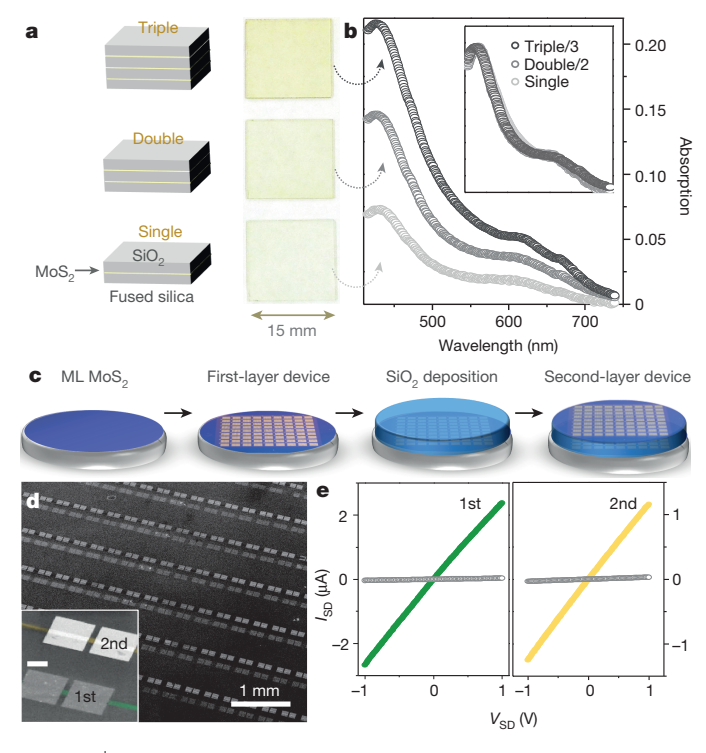


Figure 4 | Multi-stacking of MoS₂/SiO₂ structure. a, Diagrams (left) and optical images (right) of single, double and triple stacking of monolayer MoS₂/SiO₂. b, Optical absorption spectra for single, double and triple stacks, respectively (normalized spectra shown in the inset). c, Diagram for fabrication of MoS₂ device/SiO₂ stacking by alternating MOCVD growth, device fabrication with photolithography, and SiO₂ deposition. See the text for details. d, False-colour SEM image of MoS₂ FET arrays on first (bottom) and second (top) layers (the inset shows an enlarged image of a pair of devices in the same relative positions as in the main panel; scale bar, 50 µm). e, $I_{\rm SD}$ – $V_{\rm SD}$ curves measured from two neighbouring devices on the first (left) and second (right) layers, both showing n-type conductance switching. For the first layer, $V_{\rm BG} = 50 \, {\rm V}$ (green) and $-50 \, {\rm V}$ (grey); for the second layer, $V_{\rm BG} = 100 \, {\rm V}$ (yellow) and $-100 \, {\rm V}$ (grey).

(an example of the latter would be the different graphene growth modes on copper and nickel), its use is not limited to the TMDsubstrate combinations reported here. Instead, it could be generalized for producing various TMD materials, both semiconductor (for example MoSe₂ or WTe₂) and metal (for example NbSe₂ or TaS₂), with precise layer control over a large scale. Indeed, our data show that, as an initial demonstration, monolayer TMD growth is possible on a variety of other technologically important substrates (such as Al₂O₃, SiN and HfO₂) with the same growth conditions as those developed for SiO₂ (see Supplementary Fig. 16 for MoS₂ growth and device fabrication on these substrates, using these nonoptimized conditions). Our versatile MOCVD growth therefore provides a new avenue for the growth, patterning and integration of multiple high-quality monolayer TMD films with different compositions and electrical properties on a single substrate, enabling the future development of atomically thin integrated circuitry.

Received 25 November 2014; accepted 13 March 2015.

- Rogers, J. A., Someya, T. & Huang, Y. Materials and mechanics for stretchable electronics. Science 327, 1603–1607 (2010).
- Ko, H. et al. Ultrathin compound semiconductor on insulator layers for highperformance nanoscale transistors. Nature 468, 286–289 (2010).
- Mitzi, D. B., Kosbar, L. L., Murray, C. E., Copel, M. & Afzali, A. High-mobility ultrathin semiconducting films prepared by spin coating. *Nature* 428, 299–303 (2003).
- Geim, Á. K. & Grigorieva, I. V. Van der Waals heterostructures. Nature 499, 419–425 (2013).

- Kaasbjerg, K., Thygesen, K. S. & Jacobsen, K. W. Phonon-limited mobility in n-type single-layer MoS₂ from first principles. *Phys. Rev. B* 85, 115317 (2012)
- Baugher, B. W. H., Churchill, H. O. H., Yang, Y. & Jarillo-Herrero, P. Intrinsic electronic transport properties of high-quality monolayer and bilayer MoS₂. Nano Lett. 13, 4212–4216 (2013).
- Radisavljevic, B. & Kis, A. Mobility engineering and a metal-insulator transition in monolayer MoS₂. Nature Mater. 12, 815–820 (2013).
- Schmidt, H. et al. Transport properties of monolayer MoS₂ grown by chemical vapor deposition. Nano Lett. 14, 1909–1913 (2014).
- Jariwala, D. et al. Band-like transport in high mobility unencapsulated single-layer MoS₂ transistors. Appl. Phys. Lett. 102, 173107 (2013).
- Ovchinnikov, D. et al. Electrical transport properties of single-layer WS₂. ACS Nano 8, 8174–8181 (2014).
- 11. Ye, Z. et al. Probing excitonic dark states in single-layer tungsten disulphide. *Nature* **513**, 214–218 (2014).
- 12. Feng, Q. et al. Growth of large-area 2D $MoS_{2(1-x)}Se_{2x}$ semiconductor alloys. Adv. Mater. **26**, 2648–2653 (2014).
- Mak, K. F., Lee, C., Hone, J., Shan, J. & Heinz, T. F. Atomically thin MoS₂: a new direct-gap semiconductor. *Phys. Rev. Lett.* 105, 136805 (2010).
- Wu, W. et al. Piezoelectricity of single-atomic-layer MoS₂ for energy conversion and piezotronics. Nature 514, 470–474 (2014).
- Mak, K. F., McGill, K. L., Park, J. & McEuen, P. L. The valley Hall effect in MoS₂ transistors. Science 344, 1489–1492 (2014).
- Lin, Y.-C. et al. Wafer-scale MoS₂ thin layers prepared by MoO₃ sulfurization. Nanoscale 4, 6637–6641 (2012).
- Song, I. et al. Patternable large-scale molybdenium disulfide atomic layers grown by gold-assisted chemical vapor deposition. Angew. Chem. Int. Ed. 53, 1266–1269 (2014).
- Najmaei, S. et al. Vapour phase growth and grain boundary structure of molybdenum disulphide atomic layers. Nature Mater. 12, 754–759 (2013).
- Van der Zande, A. M. et al. Grains and grain boundaries in highly crystalline monolayer molybdenum disulphide. Nature Mater. 12, 554–561 (2013).
- Lee, Y.-H. et al. Synthesis and transfer of single-layer transition metal disulfides on diverse surfaces. Nano Lett. 13, 1852–1857 (2013).
- 21. Liu, H. et al. Statistical study of deep submicron dual-gated field-effect transistors on monolayer chemical vapor deposition molybdenum disulfide films. *Nano Lett.* **13**, 2640–2646 (2013).
- 22. Yu, Y. et al. Controlled scalable synthesis of uniform, high-quality monolayer and few-layer MoS₂ films. Sci. Rep. **3**, 1866 (2013).
- Zhang, Y. et al. Controlled growth of high-quality monolayer WS₂ layers on sapphire. ACS Nano 7, 8963–8971 (2013).
- 24. Zhao, W. et al. Evolution of electronic structure in atomically thin sheets of WS $_2$ and WS $_2$. ACS Nano **7**, 791–797 (2013).
- Li, H. et al. From bulk to monolayer MoS₂: evolution of Raman scattering. Adv. Funct. Mater. 22, 1385–1390 (2012).
- Berkdemir, A. et al. Identification of individual and few layers of WS₂ using Raman spectroscopy. Sci. Rep. 3, 1755 (2013).
- King, D. A. & Woodruff, D. P. Growth and Properties of Ultrathin Epitaxial Layers (Elsevier, 1997).
- Connor, R. & Adkins, H. Hydrogenolysis of oxygenated organic compounds. J. Am. Chem. Soc. 54, 4678–4690 (1932).
- Cristol, S. et al. Theoretical study of the MoS₂ (100) surface: a chemical potential analysis of sulfur and hydrogen coverage. J. Phys. Chem. B 104, 11220–11229 (2000).
- Najmaei, S. et al. Electrical transport properties of polycrystalline monolayer molybdenum disulfide. ACS Nano 8, 7930–7937 (2014).

Supplementary Information is available in the online version of the paper.

Acknowledgements We thank P. L. McEuen, M.-H. Jo, H. Heo and H.-C. Choi for discussions, and M. Guimaraes and Z. Ziegler for help in preparing the manuscript. This work was supported mainly by the AFOSR (FA2386-13-1-4118 and FA9550-11-1-0033) and the Nano Material Technology Development Program through the National Research Foundation of Korea (NRF) funded by the Ministry of Science, ICT, and Future Planning (2012M3A7B4049887). Additional funding was provided by the National Science Foundation (NSF) through the Cornell Center for Materials Research (NSF DMR-1120296) and by the Samsung Advanced Institute for Technology GRO Program. Device fabrication was performed at the Cornell NanoScale Facility, a member of the National Nanotechnology Infrastructure Network, which is supported by the National Science Foundation (ECS-0335765).

Author Contributions K.K. and S.X. contributed equally to this work. K.K, S.X. and J.P. conceived the experiments. K.K. and S.X. performed the synthesis, optical characterization, device fabrication, and electrical measurements. L.H. conducted low-temperature electrical measurement, with assistance from K.F.M. Y.H, P.Y.H. and D.A.M. performed atomic resolution STEM imaging. K.K. carried out DF-TEM and data analysis, with assistance from C.-J.K. K.K, S.X. and J.P. wrote the manuscript. All authors discussed the results and commented on the manuscript.

Author Information Reprints and permissions information is available at www.nature.com/reprints. The authors declare no competing financial interests. Readers are welcome to comment on the online version of the paper. Correspondence and requests for materials should be addressed to J.P. (jpark@cornell.edu).

SUPPLEMENTARY METHODS

MOCVD growth of ML MoS₂ and WS₂ films. As illustrated in Fig. 2a, the synthesis of ML MoS₂ and WS₂ was carried out in a 4.3-inch (inner diameter) hot-wall quartz tube furnace. Molybdenum hexacarbonyl (MHC), tungsten hexacarbonyl (THC), diethyl sulphide (DES), which have high equilibrium vapour pressure near room temperature, are selected as chemical precursors for Mo, W, S, respectively, and introduced to the furnace in gas phase. H₂ and Ar are injected to the chamber using separate lines. All the precursors used in our MOCVD growth are commercially available with well-documented safety protocols (MHC: Sigma Aldrich 577766, THC: Sigma Aldrich 472956, DES: Sigma Aldrich 107247). The safety ratings for these precursors require them to be handled inside of a fume hood. (MHC, THC: NFPA rating for health hazard 4, DES: NFPA rating for health hazard 2). The optimum growth parameters for ML MoS₂ and WS₂ films are as follows. We use a total pressure of 7.5 Torr, growth temperature of 550 °C and growth time (t_0) of 26 hrs. The flow rate of precursors are 0.01 sccm for MHC or THC, 0.4 sccm for DES, 5 sccm for H₂, and 150 sccm for Ar, which were regulated by individual mass flow controllers (MFCs). The low flow rates were used for MHC, THC and DES for the layer-by-layer growth mode. The long growth time ($t_0 \sim 26$ hrs), is necessary for full ML growth, because of the low growth rate in this regime. NaCl is loaded in the upstream region of the furnace as a desiccant to dehydrate the growth chamber, which significantly increases the grain size, as discussed in Fig. S6. We use a 4-inch fused silica wafer or a 4-inch Si wafer with 285 nm thick thermal SiO₂ as the main growth substrates. Also the growth is possible on Al₂O₃, HfO₂, and SiN (see Fig. S16).

Optical measurements. Film patterning: Photolithography was performed to make the holearray pattern on the MoS₂ film, where a sacrificial layer of PMMA A4 is coated before the photoresist. O_2 plasma (400 W, 300 s) was used to remove the unwanted MoS_2 and sacrificial PMMA from the SiO_2 surface. The chips were then placed in acetone for 3 hours to thoroughly remove the photoresist and the PMMA residue.

Optical absorption: The absorption measurements were performed with a Shimadzu UV-Vis-NIR Spectrometer under ambient conditions. All measured samples were grown on a fused silica substrate, and a bare fused silica substrate was used as the reference.

Photoluminescence: The photoluminescence (PL) measurements were performed with a 532 nm excitation laser under ambient conditions. The PL spectra from the sample were collected by an imaging spectrometer with a CCD camera, and the PL images were taken directly using band pass filters with the centre wavelength corresponding to 1.9eV for MoS₂ and 2.0 eV for WS₂.

TEM analysis. Sample preparation: The ML MoS₂ film grown on a SiO₂/Si substrate was coated by PMMA A2 or A4, and then the substrate was etched in KOH 1M solution at 90 °C. After being rinsed in deionized water three times, the PMMA supported MoS₂ film was transferred to a TEM grid, and the chip was annealed in an ultra-high vacuum (10⁻⁷ Torr) or atmospheric pressure with Ar (100 sccm) and H₂ (100 sccm) flow at 350 °C for 3 hours in order to remove the PMMA¹⁹

DF-TEM: DF-TEM images, along with electron diffraction patterns, were taken using an FEI Tecnai T12 Spirit, operated at 80 keV. The acquisition time for each dark field image was 10 seconds.

ADF-STEM: ADF-STEM images were taken using a Nion Ultra STEM 100 operated at 60 keV. The convergence angle was 30 mrad, and the probe current was about 50 pA.

Device fabrication. For the FET fabrication, we start with an as-grown ML TMD film on 285 nm SiO₂/Si and first define the source and drain electrodes using the standard photolithography

process, followed by e-beam evaporation of 0.5 nm Ti/75 nm Au. After lifting off using Microposit Remover 1165, we then define and etch the conducting channel for FET devices using photolithography and O₂ plasma etching. For top gate fabrication, 30 nm HfO₂ is deposited using atomic layer deposition (ALD) as the dielectric material, followed by the same electrode fabrication process for top-gate electrode fabrication (for top gate WS₂ FETs, we deposit 1 nm Al₂O₃ as the seeding layer for HfO₂ ALD). We also deposit 30 nm HfO₂ on top of the back gated devices. This increases the carrier doping level and the conductance of our devices, enabling reproducible measurements under ambient conditions (see Fig. S17). All devices shown in Fig. 3 and 4 were fabricated using standard photolithography techniques, except for the additional voltage probes (the five thin electrodes in Fig. 3a, inset) which were added later using e-beam lithography. The dimensions (W, width and L, length) of conducting channels are as follows: W 15 μm (Fig. 3a-3c), W 9 μm, L 19 μm (Fig. 3d and 3g), W 7.7 μm, L 3.3 μm (Fig. 3e), W 7.7 μm, L 5.3 μm (Fig. 3f), W 15 μm, L 15 μm (Fig. 4d and 4e). For the fabrication of the multistacked device in Fig. 4, the SiO₂ consists of three successive depositions: 100 nm SiO₂ was deposited using PECVD at 30 W and 200 °C, followed by 350 nm SiO₂ deposited using PECVD at 140 W and 350 °C, and 50 nm SiO₂ deposited using ALD at 200 °C.

Electrical measurements. All the electrical measurements (except for Fig. 3c) were done under ambient conditions using a custom-built probe station with an Agilent B1500 Device Analyzer. Both four-probe and two-probe measurements were used to accurately measure the sheet conductance. Comparing the results of four-probe and two-probe measurements, the contact resistivity is estimated to be approximately $50 \Omega \cdot mm$. For temperature dependent measurements (Fig. 3c), FET devices were wirebonded and measured in a cryostat in vacuum for temperatures down to 77K.

SUPPLEMENTARY NOTES

A. Growth mechanism of layer-by-layer (LBL) growth

We have conducted two experiments to support LBL growth mechanism. First, Fig. S3 presents optical reflection (OR), PL and SEM images taken from our MOCVD grown ML MoS2 films (average grain size $\sim 3 \mu m$) after different growth times (0.8 t₀, 1.0 t₀, and 1.5 t₀). It confirms that additional nucleation on the existing first layer does not occur until the first layer growth is completed and the growth proceeds by enlarging the already-nucleated grains for $t < t_0$, most likely by edge attachment growth. After t₀ (full first layer growth), the nucleation for the second layer occurs at the grain boundaries (GBs) and in the basal plane. The PL intensity images show striking behaviours especially at the GBs. They show much brighter PL uniformly along GBs at t = t_0 and much darker PL there when $t > t_0$. The brighter PL at $t = t_0$ is consistent with the PL behaviours previously seen from the tilt GBs in CVD grown MoS₂¹⁹. This suggests that upon the completion of the first layer growth ($t = t_0$), neighbouring grains are uniformly connected laterally by tilt GBs before further growth occurs for the second layer. Once the second layer starts growing on top of the first layer, the PL signal decreases especially along GBs, as the band structure of MoS₂ shifts from direct bandgap (ML) to indirect bandgap (for multilayers). Altogether, our data in Fig. S3 confirm the LBL growth mode in our MOCVD growth and the high-quality uniform intergrain connection at the optimum growth time (t_0) . We also note that monitoring PL enhancement along GBs can be used in the future to find the optimum growth time t₀ and to confirm the high quality intergrain connection in the grown film.

The edge attachment growth mechanism for our MOCVD growth is further supported by Fig. S4. Here, we performed a partial growth of ML MoS_2 (step I; $t < t_0$) and re-growth (step II),

where the step II was conducted on the same sample generated after step I. The same film was characterized by optical reflection, PL, DF-TEM after each growth step to observe the location and morphologies of the growth. Our data confirm that during the re-growth, MoS_2 grains continue to grow by edge attachment without generating additional nucleation sites on available SiO_2 surfaces. This is confirmed by the same average number of nuclei (or grains in the first layer) per unit area after step I and step II (0.27 $\mu m^{-2} \rightarrow 0.26 \mu m^{-2}$), again indicating that the empty space after step I was completely filled by continued growth of existing grains (along their edges) with the same crystal orientation without creating additional grains.

B. Thermal decomposition of precursors

We studied thermal reaction for DES and MHC using a residual gas analyser (RGA), which connected to the outlet of the furnace and detects the mass signal of the gas residue. Fig. S5 shows the relative intensity ratio for corresponding molecules extracted from mass spectra of RGA. First, we flowed vaporized MHC into the chamber at room temperature (blue circle), and we confirmed that vaporized MHC contains several carbonyl molybdenum, $Mo(CO)_x$. Above 250 °C the signal for $Mo(CO)_x$ disappeared, indicating that $Mo(CO)_x$ was completely decomposed. In the case of DES, the intensity profiles at room temperature (blue circle) are almost the same as at growth temperature, 550 °C (red circle), with both showing various hydrocarbon sulphides (C_xH_yS) under RGA resolution. This means that the concentration of DES in the furnace barely changed due to its decomposition. According to the RGA study, we summarize the status of precursors at growth temperature: i) the concentration of C_xH_yS is uniform inside the furnace at the laminar flow condition. ii) MHC is decomposed to Mo and delivered by high flow Ar.

C. Dependence of grain size on concentration of H₂, H₂O, and DES

We have already shown the H₂ concentration dependence of grain size in Fig. 2d. The dependence on H₂O concentration was observed under the presence of salt desiccant (NaCl, KCl, NaBr), as shown in Fig. S6a, where the grain size increased up to 100-fold, according to the presence/absence of salt. Also, Fig. S6b shows that the concentration of DES affects the grain size.

In order to explain these phenomena, we need to discuss the precursor decomposition and nucleation kinetics. First, according to hydrolysis and hydrogenolysis²⁸, H₂ and H₂O promote the decomposition of DES precursor, which enhances the concentration of sulphur vapour. Also, the concentration of sulphur vapour linearly depends on the concentration of DES, since DES contains certain ratio of sulphur vapour. Second, the concentration of sulphur affects the nucleation kinetics and grain size. The assumptions we make are: (i) our growth is Mo diffusion limited growth, since the Mo concentration is kept low for layer-by-layer growth. In comparison, the concentration of DES is much higher than that of Mo vapour. (ii) when a Mo atom produced by thermal decomposition of MHC, arrives at the surface, it diffuses until reacting with sulphur produced by decomposition of DES. (iii) energetically, Mo and S atoms prefer to be adsorbed at a MoS₂ edge. (iv) if the decomposition rate of DES is fast, Mo atoms lose their chance to find energetically favourable positions and nucleation occurs at a non-edge region. Based on these assumptions, we conclude that the nucleation density of MoS_2 increases on the surface when the decomposition kinetics of DES becomes faster. Therefore, when H₂, H₂O, and DES concentrations are high, nucleation density increases and grain size decreases.

SUPPLEMENTARY FIGURES

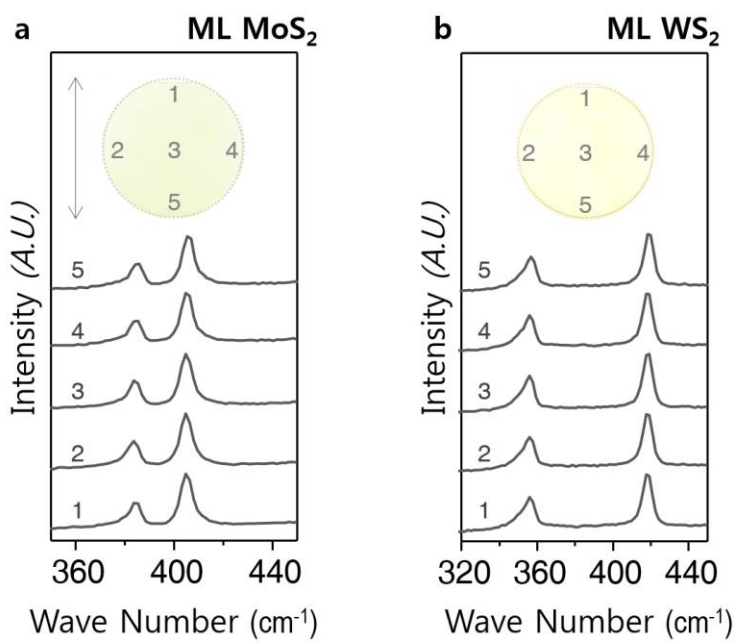


Fig. S1 | Raman spectra for MoS_2 (a) and WS_2 (b) respectively, taken at different locations marked on the corresponding fused silica wafer.

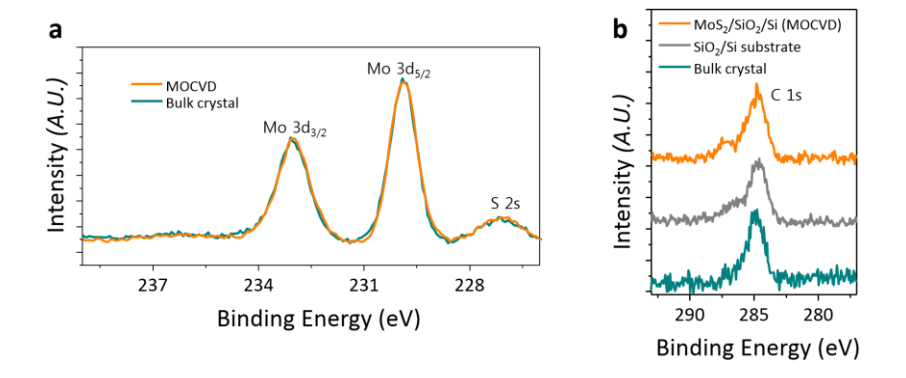


Fig. S2 | XPS spectra of **a**, Mo 3d 3/2, 5/2 and S 2s state for MoS_2 grown by our method (orange) and bulk MoS_2 single crystal (cyan blue), where the peak position and FWHM are almost identical. **b**, C 1s for MoS_2 grown by our method (orange), bare SiO_2/Si substrate after solvent cleaning (grey) and bulk single crystal (cyan blue), where all three sample show similar peak area of C 1s, which means our films do not contain significant carbon residue after MOCVD process (curves shifted from the bottom for clarity).

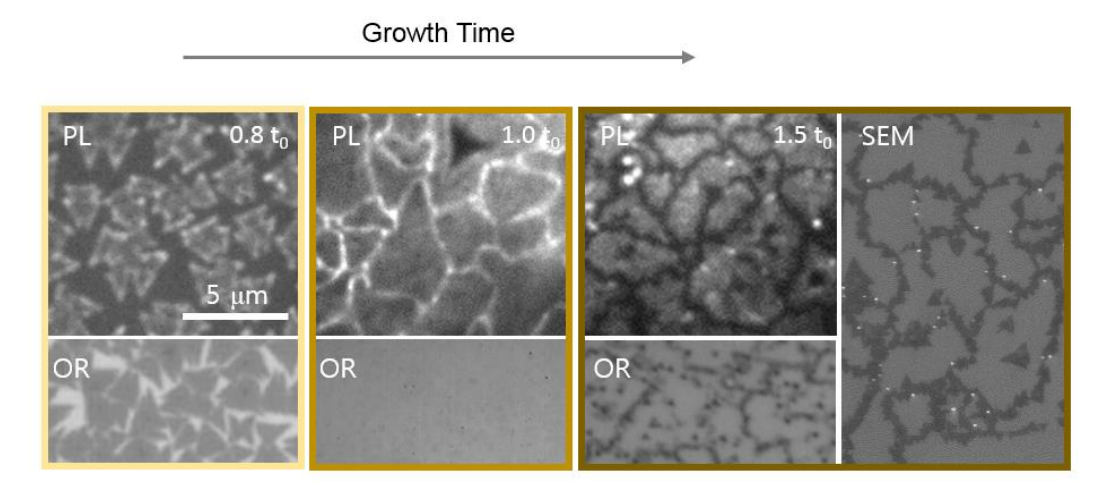


Fig. S3 | Optical reflection, PL, SEM images of MOCVD-grown MoS_2 at different growth times, where t_0 is the optimal growth time for full ML coverage.

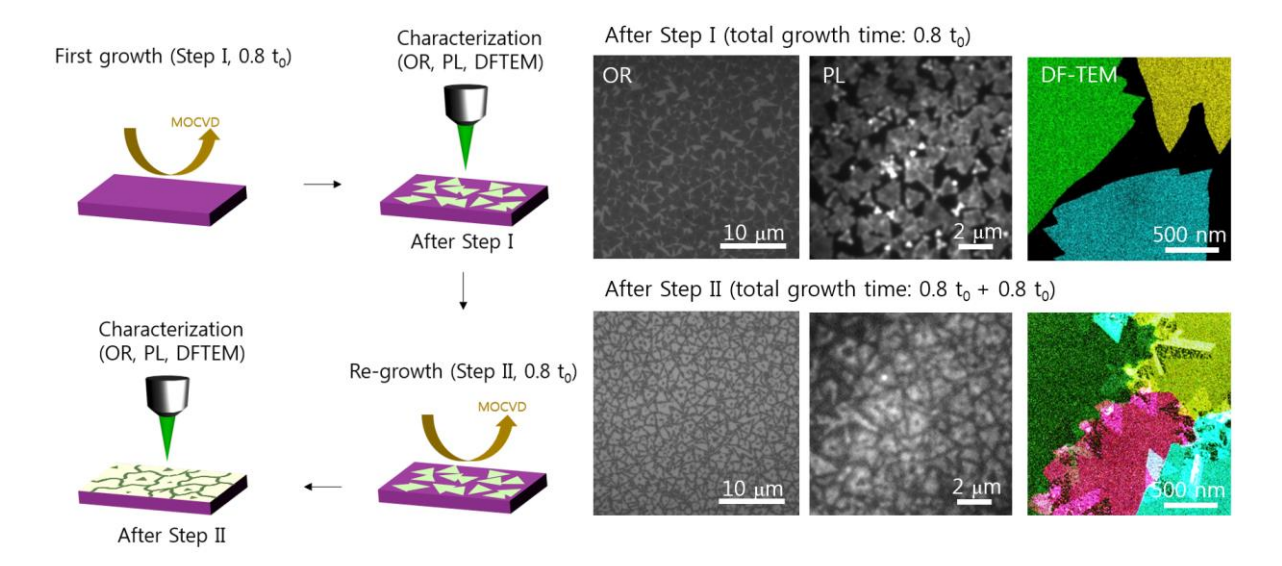


Fig. S4 | Schematics of growth (step I) and re-growth (step II) of MoS₂ film and corresponding optical reflection, PL, DF-TEM images.

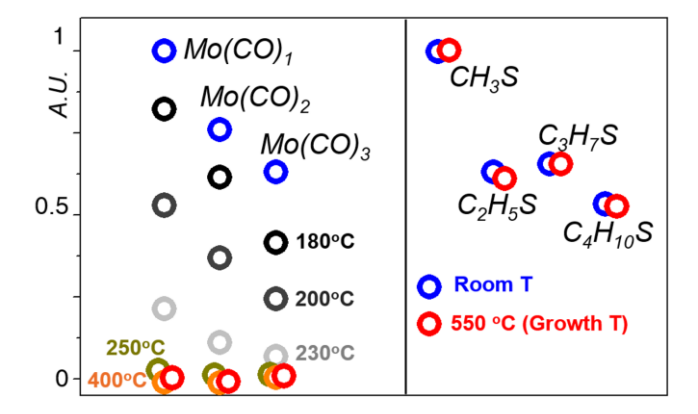


Fig. S5 Normalized intensity of residual gas signal for $Mo(CO)_x$ and C_xH_yS depending on temperature. Each dot corresponds to a temperature, as denoted in the figure.

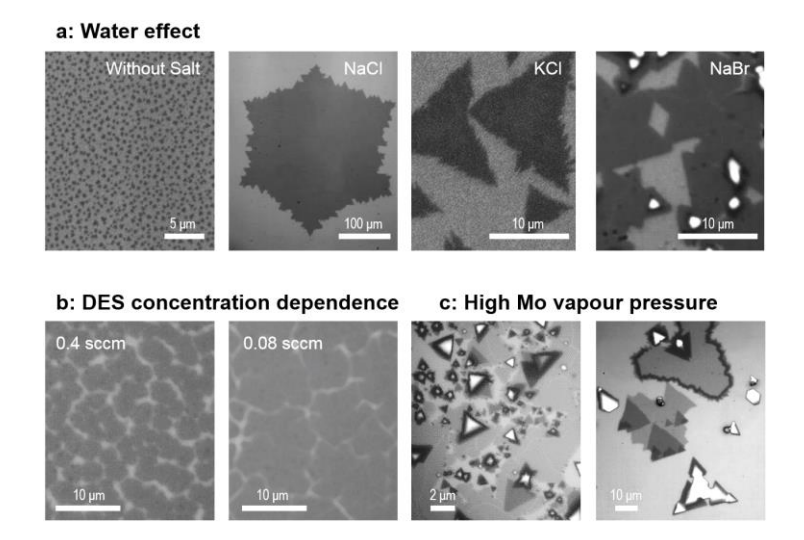


Fig. S6 | Morphology change of MOCVD-grown MoS_2 depending on the growth parameters. In order to show grain size clearly, we intentionally grow partially covered MoS_2 . **a,** salt (desiccant) dependence of grain size. **b,** DES flow rate dependence of grain size. **c,** high Mo vapour concentration environment, where a mixture of monolayer, multilayer and no-growth regions exist.

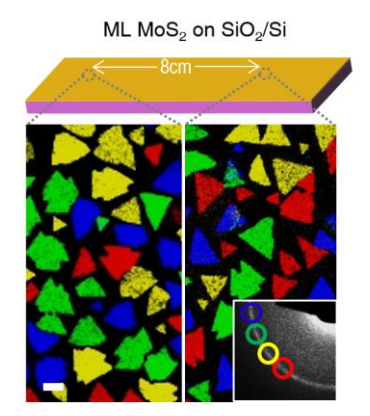


Fig. S7 | False-colour DF-TEM image of MoS₂ grown at two locations 8 cm apart, where the identical grain size and nucleation density suggests the homogeneous nucleation over the whole growth area. Scale bar, 100 nm.

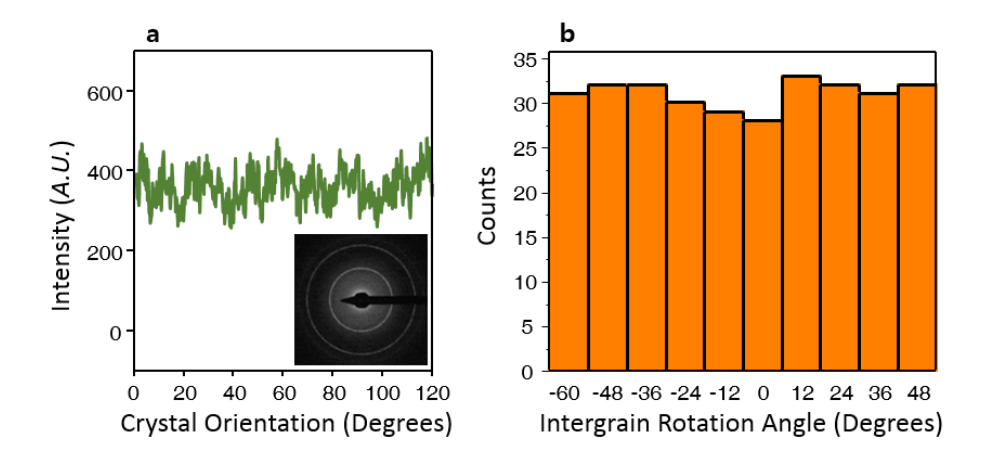


Fig. S8 | **a,** A polar plot of the electron diffraction intensity (diffraction map shown in the inset) measured from a large area ML MoS₂ (inset), indicating a uniform angular distribution of the MoS₂ crystal orientation³². It is generated by averaging the diffraction intensity from the three equivalent angular domains, each spanning 120 degrees. **b,** A histogram of intergrain rotation angles measured from all grain boundaries found in the ML MoS₂ sample shown in **Figure 2e**, suggesting no preferred intergrain tilt angle. For this, the crystal orientation for every MoS₂ grain was first obtained from five DF-TEM images taken with different objective aperture locations (each centred at 0°, 12°, 24°, 36° and 48°, respectively)³². In each DF-TEM image taken at an objective aperture location θ, we assign the crystal orientation of θ (for brighter regions; from aligned Mo sub-lattice) or θ - 60° (for less bright regions; from aligned S sub-lattice)¹⁹. The intergrain rotation angles were extracted using these assignments and range between -60° to 60° (with ± 6° error).

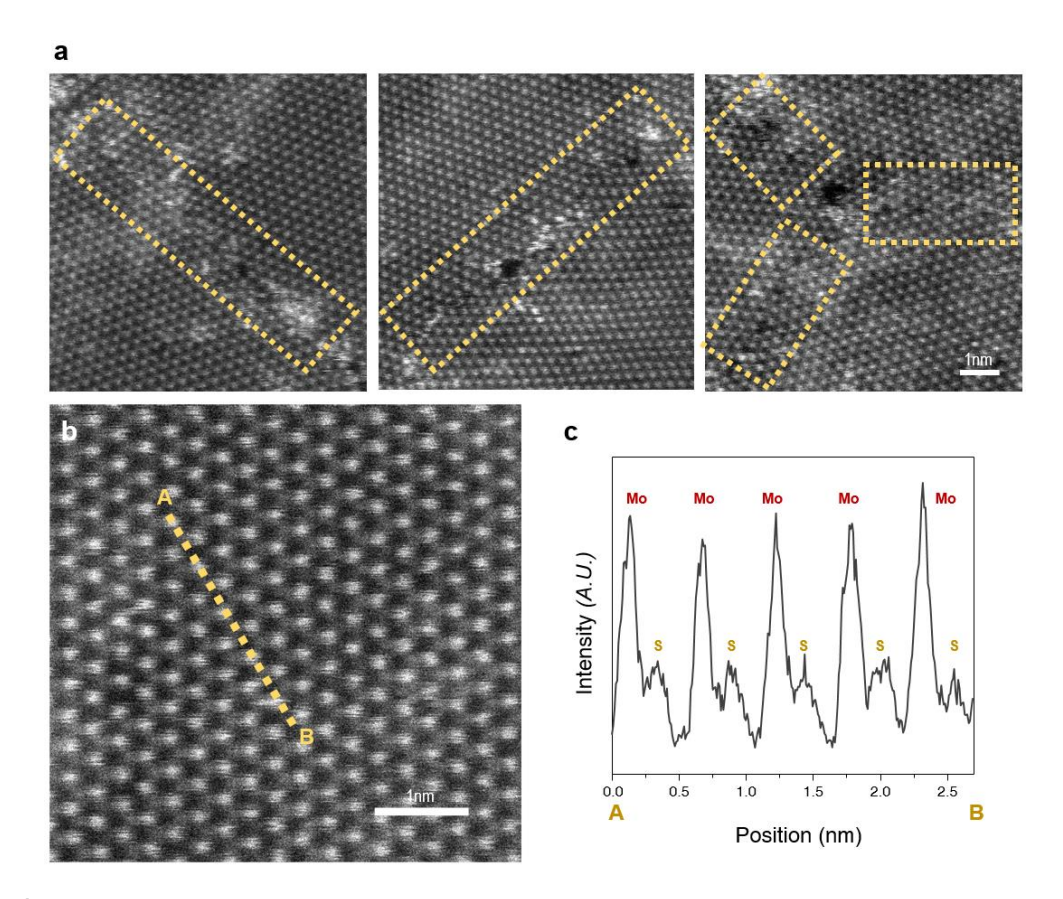


Fig. S9 | a, ADF-STEM images of laterally-stitched grain boundaries in a ML MoS₂ film. The sub nanometre holes come from electron beam radiation damage, and the clouds are surface contaminations generated during the transfer process. b, High quality ADF-STEM image of ML MoS₂ film and c, corresponding line profile of intensity. The image intensity is roughly proportional to Z^{γ} , where Z is the atomic number, and $1.3 < \gamma < 2$.

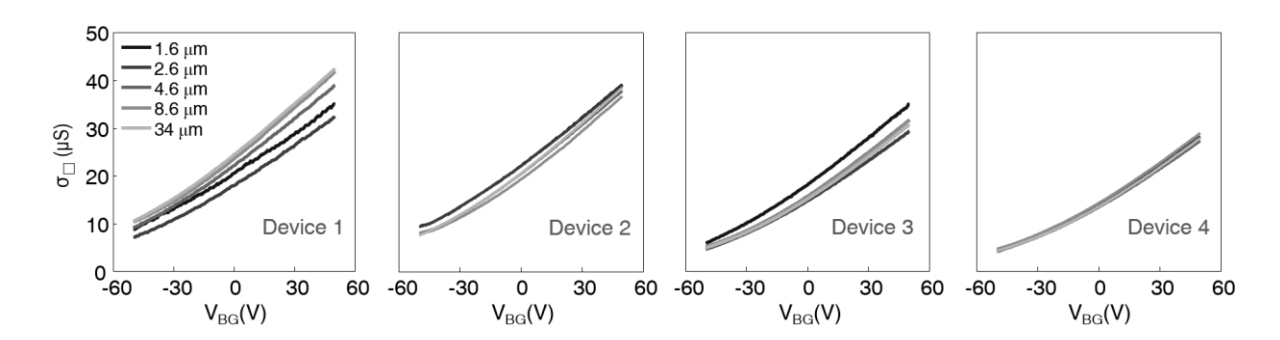


Fig. S10 | Gate-dependent σ_{\square} of four multiple-electrode ML MoS₂ FETs (same geometry as shown in Fig. 3a inset) separated by up to 3.3 mm.

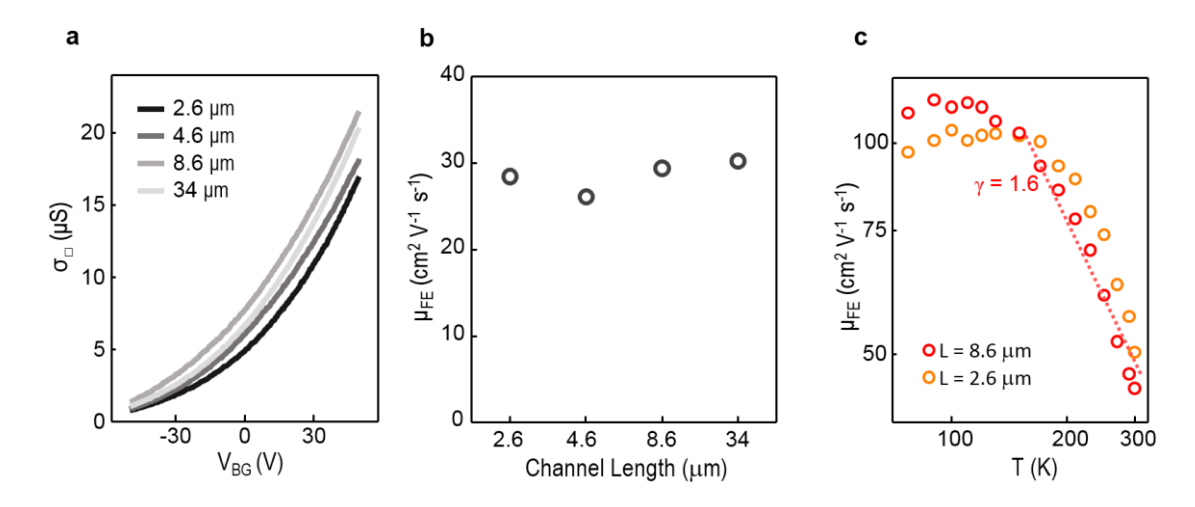


Fig. S11 | a, Transfer curves measured from MoS_2 of grain size 3 μ m with different channel lengths. b, Field effect mobility (μ_{FE}) of different channel lengths extracted from (a). c, Temperature dependence of μ_{FE} measured from MoS_2 film of grain size 3 μ m, with different channel lengths, which show the same dependence as shown in Fig. 3c.

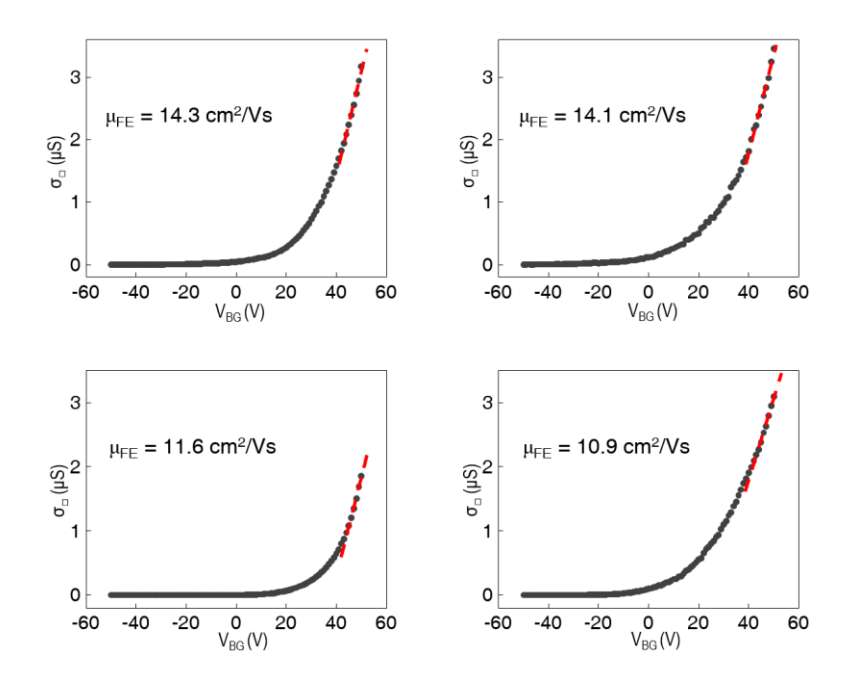


Fig. S12 | Gate-dependent two-terminal σ_{\square} of four additional ML WS₂ FETs, of which the extracted mobilities are 14.3, 14.1, 11.6 and 10.9 cm²/Vs, respectively.

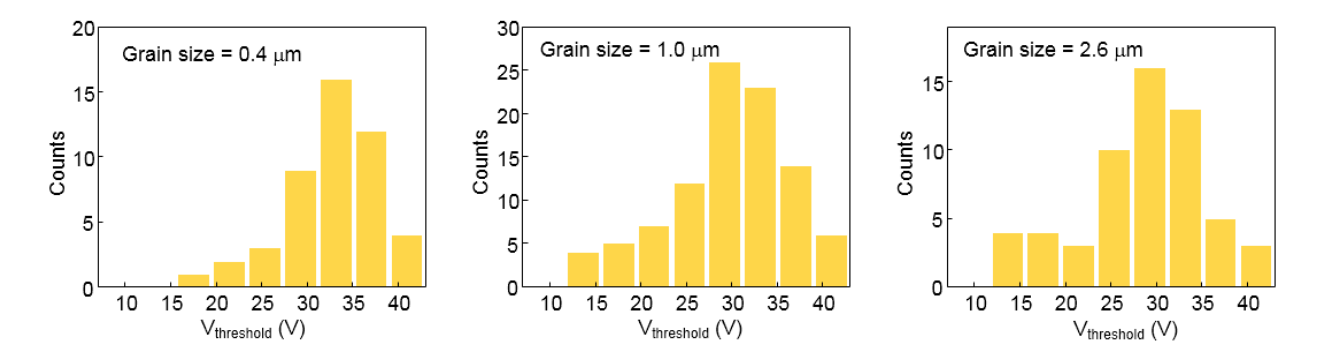


Fig. S13 | Histograms of threshold voltage of MoS_2 FETs with grain size 0.4, 1.0 and 2.6 μ m, respectively.

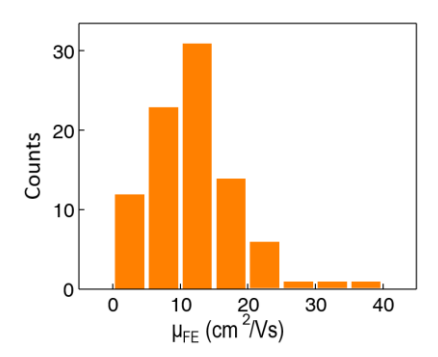


Fig. S14 | Statistics for field effect mobility of MoS₂ FETs taken from the devices in Fig. 3g.

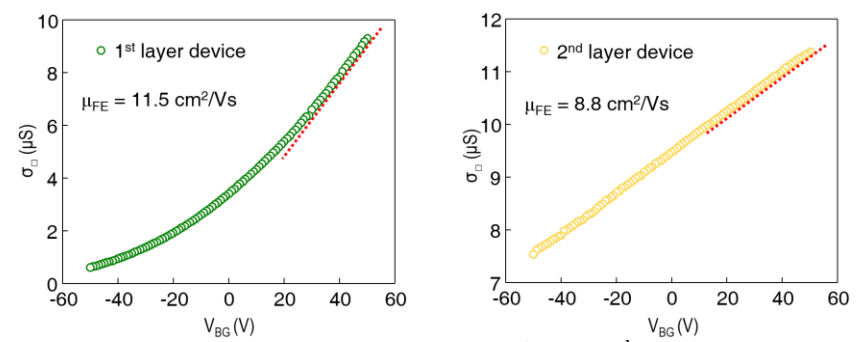


Fig. S15 | Gate-dependent σ_{\square} for ML MoS₂ FET on 1st and 2nd layer in the multi-stacked device structure. The total gate oxide (SiO₂) thickness for 1st and 2nd layer devices are 285 nm and 785 nm, respectively.

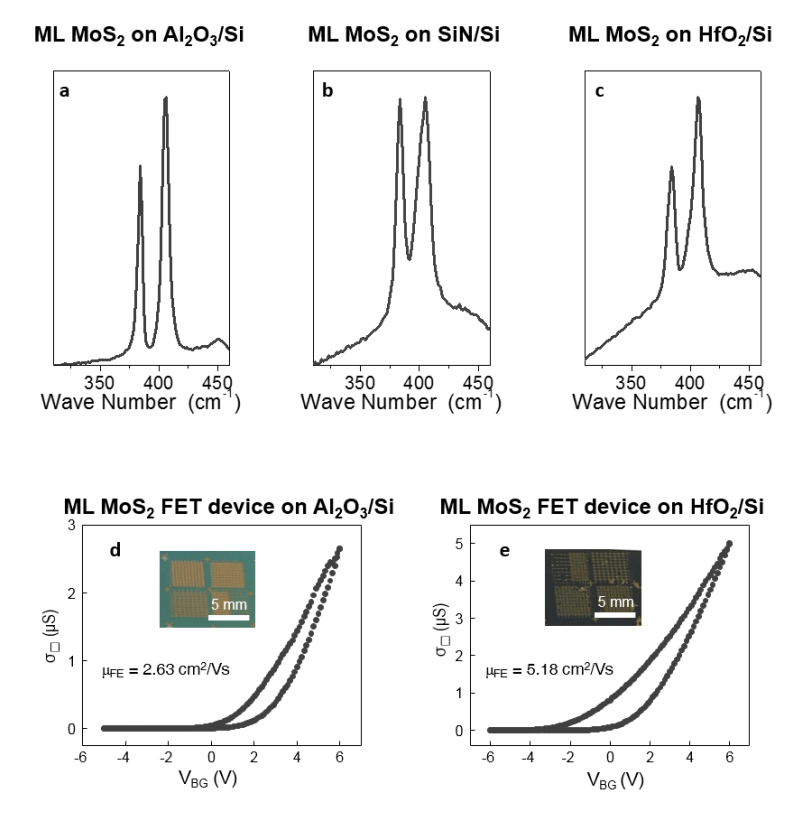


Fig. S16 | **a-c,** Raman spectra for MoS_2 grown on Al_2O_3 , SiN and HfO_2 covered Si, respectively. **d-e,** σ_{\square} - V_{BG} curves for ML MoS_2 FET on Al_2O_3/Si and HfO_2/Si , respectively. The measured dielectric constant for Al_2O_3 and HfO_2 is 6.0 and 15.5, respectively. These MoS_2 films were grown under the same conditions developed for SiO_2 substrates as described in Methods, without any further optimization.

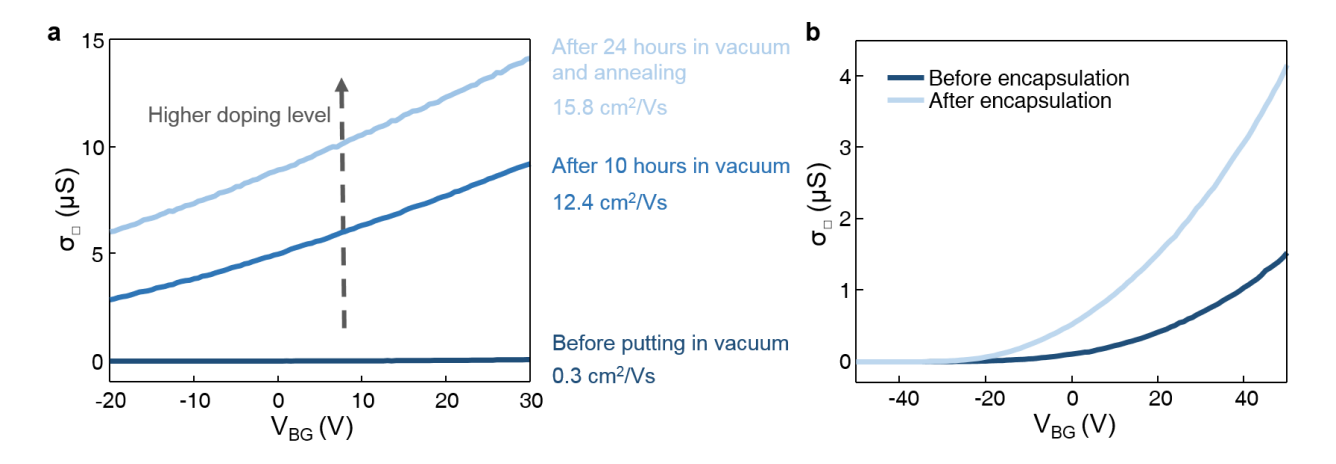


Fig. S17 | \mathbf{a} , The effect of measuring in vacuum and annealing on the device's electrical performance (the vacuum and annealing n-dope the MoS₂ devices). \mathbf{b} , The transfer property of same device in ambient before and after HfO₂ encapsulation (encapsulation n-dopes MoS₂).

REFERENCES

- 31. Havener, R. W. *et al.* High-throughput graphene imaging on arbitrary substrates with widefield Raman spectroscopy. *ACS Nano* **6,** 373–80 (2012).
- 32. Huang, P. Y. et al. Grains and grain boundaries in single-layer graphene atomic patchwork quilts. *Nature* **469**, 389–392 (2011).